Nanoscale

PAPER

View Article Online
View Journal | View Issue

Cite this: *Nanoscale*, 2025, **17**, 18143

Sensing relative humidity with a fluorescent seed-like biodegradable flier†

Albenc Nexha, [a] Stefano Mariani, [b] Kliton Cikalleshi, [b,c] Thomas Kister, [a] Barbara Mazzolai *[b] and Tobias Kraus *[a,d]

Received 31st March 2025,
Accepted 4th July 2025

DOI: 10.1039/d5nr01318f

rsc.li/nanoscale

Plant-inspired soft robots enable distributed environmental monitoring. Fliers, *i.e.* soft robots that are carried passively by the wind, can be effectively deployed and cover large areas and distances. State-of-the-art fliers for humidity sensing are largely composed of electronic components, which increase cost and generate electronic waste. Here, we introduce self-deployable and biodegradable fliers inspired by natural *Ailanthus altissima* seeds. These artificial fliers are composed of fluorescent, cellulose-based composites with sensing capabilities. The material is shaped into artificial seeds using scalable 3D extrusion processing. Red-emitting Mn^{2+}-doped Er^{3+}, Yb^{3+}:$NaYF_4$ nanoparticles in the composite provide a strong optical emission upon excitation at 980 nm wavelength. The cellulose matrix absorbs water, which quenches the intensity of fluorescence of the nanoparticles. Increasing humidity thus changes the color of the fluorescence emission from red to green. We used ratiometric sensing to detect the humidity of the surroundings.

Introduction

Humidity impacts most facets of life. In the agricultural field, controlling the humidity levels is directly linked to the protection of crops and development of plants.[1–3] For example, elevated levels of humidity promote the growth of mold and bacteria that infect plants and can cause crops to fail.[1–3] In other scenarios, increased levels of humidity reduce air circulation, which allows pollutants to be trapped in the air.[4] This, in turn, might induce issues with the skin and the respiratory tract in humans.[5,6] Current technologies for humidity sensing largely rely on the water-dependent electrical resistance or capacitance of materials.[7–10] Such sensors provide high accuracy but require power supplies, display devices, and provide only point measurements, which hamper their applications in multiple areas. Therefore, new eco-friendly alternatives are in demand.

Wireless sensors are interesting alternatives if they can operate autonomously and enable efficient data collection.[11,12] Bioinspired wireless sensors adapt principles of organisms for aspects of the sensors. For example, passive motion triggered by the wind to distribute pollen or plant seeds can simplify deployment and add functionalities when combined with sensing units.[13] This enables their use in remote areas, for example with millimeter-scale Bluetooth radios[14,15] or backscattered communication systems.[16]

Plant-inspired soft robots (also known as fliers) have been introduced for distributed environmental sensing.[2,11,12,16–21] These fliers are inspired by seeds that after falling from the tree, start auto-rotating with the wind and either lie flat or start drilling into the soil.[22] A flier inspired by *Tragopogon pratensis* seeds has been recently introduced with a backscattered communication system as a readout unit to measure temperature, light intensity and humidity.[16] Such sensors require electronics, power sources, and sometimes additional external components too, such as crystal oscillators. They need to be retrieved from the environment at the end of their lifetime. It is crucial to develop fliers that can remain in the field where they degrade and cause no harm. This might be achieved when using non-toxic and biodegradable materials for the structural and sensor components.[2,11,12,16–21] These sensors could be read using unmanned aerial vehicles (UAVs) integrated with laser lights and hyperspectral cameras.[11,12]

Recently, seed-inspired fliers composed of biodegradable materials have been demonstrated. For example, fliers inspired by *Tristellateia australasiae*,[11] dandelions and *Acer campestre* seeds[19] were produced using poly(lactide-*co*-glycolide) as a matrix. These fliers are capable of sensing environmental parameters *via* colorimetry as a readout.[19] Other types of seeds,

[a]*INM-Leibniz Institute for New Materials, Campus D2 2, 66123 Saarbrücken, Germany. E-mail: tobias.kraus@leibniz-inm.de*
[b]*Bioinspired Soft Robotics Laboratory, Instituto Italiano di Tecnologia, Via Morego, 30, 16163 Genoa, Italy. E-mail: barbara.mazzolai@iit.it*
[c]*The Biorobotics Institute, Scuola Superiore Sant'Anna, Viale Rinaldo Piaggio 34, 56025 Pontedera, Italy*
[d]*Saarland University, Colloid and Interface Chemistry, Campus D2 2, 66123 Saarbrücken, Germany*

† Electronic supplementary information (ESI) available. See DOI: https://doi.org/10.1039/d5nr01318f

inspired by *Ailanthus altissima*[17] and *Pelargonium appendiculatum*,[2,23] were used for sensing using visual detection, for example, motion of the seeds triggered by environmental parameters.[23] The use of colorimetric readouts limits the reliability, precision, and maximal distance of the readout.[24]

From a material point of view, several limitations are noted. Refractive optical elements are limited by their angle-dependent responses. For example, the photonic crystals employed on the *Ailanthus altissima* seeds display angle-dependent colorimetric changes,[25] which renders the outdoor readout complex and leads to inaccurate data reading.[2] Other materials, such as the organic molecules (anthocyanin or spirooxazine) implemented in *Tristellateia australasiae* seeds,[11] are prone to degradation when exposed for prolonged periods of time in the sunlight and suffer from photobleaching. Other types of humidity sensors, such as flexible carbon-based materials, regardless of their fast responses, display a narrow detection range and poor cycling stability.[26] Plasmonic nanoparticles as humidity sensors have high sensitivities, however, their high cost is a limiting factor.[26]

Lanthanide-doped, upconverting fluorescent materials can overcome these limitations. Lanthanide ions can absorb multiple low-energy photons and emit at shorter wavelengths (a process called "upconversion").[27] The resulting emissions are narrow and do not photobleach,[27] with good quantum efficiencies over a wide range of temperatures from <50 K to >1000 K. Stability is retained even in strong electromagnetic fields.[27,28] Lanthanide ions display multiple emission bands with high signal-to-noise ratios when excited with an irradiation source.[27,29] Lanthanide-doped materials are generally accepted as non-toxic compounds,[30] and recently, their biodegradability has been confirmed *in vivo*.[31]

The photoluminescence of such phosphors depends on temperature and the chemical environment where the dopant ions are located. They are therefore suitable for environmental sensing.[12,27–29,32] Their temperature-dependent emission has been used in *Acer campestre* seeds that were 3D-printed from phosphor-containing composites (polylactic acid, PLA, as a polymer) using fused deposition modeling, FDM.[12] They were used to monitor the temperature of topsoil by detecting the change of the green emissions at 520 nm and 540 nm.[12] A ratiometric sensing approach was used to increase the signal-to-noise ratio. This technique is not influenced by the optical setup, concentration of the nanoparticles, or external illumination, for example, sunlight.[12,27,29]

Here, we extend the environmental sensing capabilities of materials based on upconverting particles. We engineered self-deployable artificial *Ailanthus altissima* fliers from a humidity-sensitive composite that we shaped *via* a direct and fast 3D printing process. Cellulose acetate was selected as a matrix due to the well-established 3D printing process, Direct Ink Writing (DIW),[33] and (bio)degradation properties, which were faster than PLA.[33,34] Cellulose acetate degrades when exposed to moisture. This polymer loses between 5 and 10% weight per year, depending on humidity and temperature.[35] At 53 °C, cellulose acetate films of up to 55 μm were completely degraded within 30 days.[36] Cellulose acetate fibers were visibly degraded within 2 months and completely degraded between 4 and 9 months in moist soil environments.[37] Light, especially, ultraviolet radiation shorter than 280 nm, can photochemically degrade cellulose acetate.[34] The degradation can be accelerated by the addition of titania particles.[34] These seeds display unique properties as they can auto-rotate around their longitudinal and vertical axes[38] and also move across the *xy* plane without relying on wind (*i.e.* a flight mode called tumbling).[39,40] They act as humidity sensors, as a unit of upconverting nanoparticles is integrated in them, whose intensity of the photoluminescence is affected by O–H vibration modes. The upconverting particles emit red light, which changes to green when exposed to humidity. The flier is designed to be eco-friendly and to monitor environmental parameters in a distributed fashion.

Experiments

Materials

$Er(NO_3)_3{\cdot}5H_2O$ (99.9%), $Yb(NO_3)_3{\cdot}5H_2O$ (99.9%), $Y(NO_3)_3{\cdot}6H_2O$ (99.9%), $Mn(NO_3)_2{\cdot}4H_2O$ (99.9%), NaF (99%), oleic acid (OLAC, 90%) and NaOH were purchased from Sigma-Aldrich. All chemicals were used without further purification. Cellulose acetate (MW = 30 000 g mol^{-1}) and lignin (alkaline) were purchased from Merck and TCI Europe N.V., respectively. Ethyl cyanoacrylate as a glue was purchased from Loctite, Henkel Corporation.

Synthesis of upconverting nanoparticles

The upconverting nanoparticles were synthesized using a published solvothermal protocol,[41] with slight modifications. Briefly, to a mixture of 16 mmol of oleic acid, 0.3 g of NaOH and 1.5 mL of deionized water, 0.6 mL of 0.5 M $Mn(NO_3)_2{\cdot}4H_2O$, 1 mL of 0.5 M $Y(NO_3)_3{\cdot}6H_2O$, 0.9 mL of 0.2 M $Yb(NO_3)_3{\cdot}5H_2O$ and 0.1 mL of 0.2 M $Er(NO_3)_3{\cdot}5H_2O$ were added under continuous stirring. Then, 4 mmol of NaF was dissolved in 2 mL of deionized water, and was added dropwise to the mixture. After stirring for 0.5 h at room temperature, the dispersion was transferred into a 25 mL Teflon-lined autoclave reactor and heated at 200 °C for 8 h. After this, the system was cooled down to room temperature. The upconverting particles were collected after washing several times with ethanol, followed by centrifugation and redispersion in an apolar solvent (*n*-hexane).

An acidic treatment was applied to remove the oleates from the surface of the upconverting nanoparticles.[42] In short, 1 mL of an *n*-hexane dispersion of the oleate-capped upconverting nanoparticles (10 mg mL^{-1}) was precipitated by adding ethanol and redispersed in 2 mL of an HCl solution (0.1 M in deionized water). The slurry was sonicated at 40 °C for 1 h to remove the oleate ligands. Then, the nanoparticles were centrifuged at 14 000 rpm for 30 min, washed three times with deionized water, and redispersed in water.

Preparation of fluorescent composites

The fluorescent composites were prepared by a solvent processing method. The composites were built of cellulose acetate and fluorescent particles. Briefly, cellulose acetate powder (500 mg) was dissolved in acetone (around 5 mL) using ultrasound and vortexing. Different concentrations of the fluorescent particles (1, 2, 5, 10, 15 and 20 wt%) were added to the dispersion upon continuous stirring. After stirring for 0.5 h, homogeneous dispersions were obtained. The dispersions were dropped into a Teflon substrate and allowed to dry at room temperature to yield a big round fluorescent composite. Composites with smaller diameters were prepared by using a Peddinghaus punch set with a dimension of 8 mm. Photographs of the composites were acquired using the camera of an iPhone 14 Pro (48-megapixel quad-pixel sensor).

Characterization of the lanthanide-doped nanoparticles and composites

The crystalline structure of the fluorescent nanoparticles was characterized *via* X-ray powder diffraction using a D8 Advance diffractometer equipped with a copper source for CuK_α radiation (λ = 1.54060 Å, 40 kV, 40 mA) operating within the 2θ range from 10° to 80°. The phonon energies of the nanoparticles were characterized by Raman spectroscopy using a Renishaw inVia microscope with a 532 nm unpolarized light within 100 to 2000 cm^{-1}. The size and shape of the samples were determined by using a transmission electron microscope (TEM, Akishima, Japan) at an acceleration voltage of 200 kV. TEM specimens were prepared by drying a drop of a diluted water dispersion of the nanoparticles on the surface of a carbon-coated copper grid. The size of the nanoparticles was determined using ImageJ software after analysing over 100 nanocrystals. Scanning electron microscopy (SEM) and energy-dispersive X-ray spectroscopy (EDX) were recorded by using a Quanta 400ESEM (FEI Technologies Inc., Oregon, USA) equipped with an EDX detector from Oxford Instruments (Abingdon, UK). An acceleration voltage between 1 kV and 15 kV was used to acquire the data. Absorbance experiments were conducted using a Cary 5000 UV-Vis-NIR spectrometer. The photoluminescence spectra of the nanoparticles and the composites were recorded using an FS5 spectrofluorometer from Edinburgh Instruments (Livingston, UK) coupled with an external NIR laser source operating at 980 nm wavelength with tunable power up to 2 W. The spectra were acquired within the wavelength range from 400 to 800 nm using a resolution of 2 nm and an integration time of 0.5 s. Digital images of the fluorescent seeds were acquired with the camera of an iPhone 14 Pro (48-megapixel quad-pixel sensor). A handheld laser pointer operating at 980 nm excitation and 300 mW (purchased from Roithner Lasertechnik GmbH, Vienna, Austria), was used to trigger the fluorescence.

Production and characterization of the fluorescent flying seeds

Natural *Ailanthus altissima* seed morphometric and aerodynamic analyses. The morphometric and aerodynamic analyses of the seeds were conducted based on a previous work.[17] Briefly, seeds of *Ailanthus altissima* were collected from a tree in Genoa, Italy. The morphometric analysis, applied to 8 samples, was conducted with the aim of extracting the longitudinal length (L_L), the transverse length (L_T), the wing thickness (T_W), the seed capsule thickness (T_S), and the diameter (D). A digital calliper (RS PRO 150 mm Digital Caliper, RS Components Ltd, UK) was used. The mass of the seeds (M) was determined with the help of an analytical balance (Practum, Sartorius AG, Germany). Wing surface area (S) was estimated using ImageJ software,[43] based on the photos of the seeds taken with the camera of a Samsung A40 smartphone (1280 × 800 pixels). The aerodynamic analysis was conducted indoors, without active ventilation. The aim was to estimate the descent speed (v_d) during the spirally twisted flight mode of the seeds. The seeds were released from a height of 2.5 m. The flight was recorded with the camera of a Samsung A40 smartphone (1280 × 800 pixels). In total, 12 seeds were analysed.

Design of the artificial *Ailanthus altissima* seeds. The artificial seeds were designed using an established approach with slight modifications.[17] Briefly, a top-view photograph of a natural seed was captured with the camera of a Samsung A40 smartphone with the resolution of 1280 × 800 pixels. From this image, a vector file of the contours of the seed was drawn using an open-source vector graphics editor (Inkscape). This vector was imported into 3D CAD modeling software (Siemens NX), where the dimensions of the artificial seeds were tuned with the goal of generating more space for the deposition of the fluorescent composite.

3D printing and characterization of the artificial *Ailanthus altissima*. The artificial *Ailanthus altissima* seeds were 3D printed using porous cellulose acetate as a substrate.[17,20] The composition of the materials for the 3D printing of the seeds was prepared by adding into a vial cellulose acetate, lignin, and acetone with the ratios of 23, 23 and 54 wt%. This solution was magnetically stirred and heated for 1 hour at 60 °C. Then, it was applied for 3D printing *via* the Direct Ink Writing (DIW) using a 3D-Bioplotter (EnvisionTEC, USA and Germany). The printing parameters were as follows: printing and build plate temperatures were set at 20 °C, speed of printing at 35 mm s^{-1} and pressure at 0.5 bar and the diameter of the nozzle was 0.4 mm. We 3D printed disks with a diameter of 13.5 mm and a thickness of 200 μm for the estimation of the porosity of the developed material after leaching and artificial *Ailanthus altissima* with a size scaled 1.5× (through volume calculation, mass measuring, and considering a density of cellulose acetate of 1.3 g cm^{-3}).[17] After solvent evaporation, the 3D printed structures were dipped in deionized water for 0.5 h prior to drying in an oven at 70 °C (repeated three times) to allow complete dissolution of the lignin and formation of the pores. The sensing unit was attached at the capsule of the printed artificial seeds using ethyl cyanoacrylate as a glue. The morphometric and aerodynamic analyses of the artificial seeds, coupled with the sensing unit, were conducted identically as described in the section "Natural *Ailanthus altissima* seed morphometric and aerodynamic analyses".

Sensing humidity with the fluorescent flying seeds

The fluorescent artificial seeds were evaluated as humidity sensors by monitoring the changes in the intensity of the photoluminescence of the lanthanide-doped nanoparticles as a function of different humidity levels. The seeds were exposed to a chamber (model ARS 380 from ESPEC Europe GmbH, Düsseldorf, Germany) with controlled levels of humidity ranging from 10% to 95%, with a flocculation level of ±2.5%. The temperature of the chamber was fixed at 25 °C. The seeds were exposed for 1 hour at a certain humidity level, and subsequently, the intensity of their photoluminescence was measured using a FS5 Edinburgh Instruments spectrofluorometer (Livingston, UK), equipped with an external NIR laser source (980 nm wavelength). The fliers were exposed to temperatures from 273 to 313 K on a cooling/heating stage (Linkam Scientific Instruments, THMS 600) and the photoluminescence spectra were recorded using the same device as for the relative humidity experiments.

Results and discussion

We created fluorescent and functional fliers inspired by natural *Ailanthus altissima* seeds. The fluorescent unit was based on upconverting Mn^{2+}-doped Er^{3+}, Yb^{3+}:$NaYF_4$ nanoparticles. The seeds can be deployed by drones equipped with a wireless controller. The seeds are carried by the wind and lie flat in the ground. Hyperspectral cameras (mounted on a drone) are then used to geolocalize the fliers on the ground. Read-out is possible with fLiDAR (fluorescence light detection and ranging) technology (Fig. S1 in the ESI†). In the following section, we discuss the synthesis of the fluorescent nanoparticles and their integration on a biodegradable matrix (cellulose acetate) to generate a composite. Next, we analyze the properties of the natural seeds to properly design the artificial seeds. We produced artificial fliers by using 3D printing technology. The optical response of the fliers to humidity was then analyzed to demonstrate their applicability for environmental sensing.

Preparation of fluorescent composites

Mn^{2+}, Er^{3+}, Yb^{3+} (30, 2, 18 mol%):$NaYF_4$ nanoparticles were synthesized using a solvothermal approach,[41] followed by ligand removal to render them water soluble.[42] The Mn^{2+} ions have two functions: doping with these ions ensures the formation of the cubic phase of the $NaYF_4$ host, and control over the color of upconversion of the Er^{3+} ions due to the resonant energy between the absorption bands of Mn^{2+} and the energy levels of Er^{3+}.[41] X-ray diffraction confirmed that the particles crystallized as a cubic phase of the $NaYF_4$ host material (Fig. 1A). The phonon energy of the host material was extracted from Raman spectroscopy under an unpolarized 532 nm laser light. The maximum phonon energy was detected at around 520 cm^{-1} (Fig. 1B), which was a relatively low value. This is a prerequisite for preparing host materials with minimum interference on the optical properties of the dopants.[27,29]

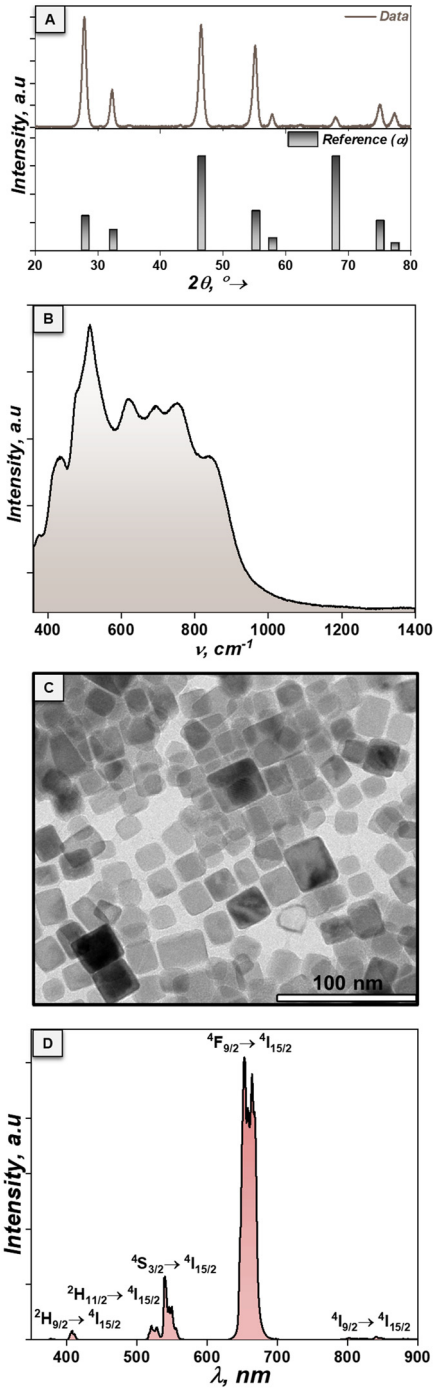

Fig. 1 Characterization of Mn^{2+}-doped Er^{3+}, Yb^{3+}:$NaYF_4$ nanoparticles: (A) X-ray powder diffraction pattern, (B) Raman spectrum under unpolarized 532 nm excitation, (C) transmission electron microscopy micrograph, and (D) photoluminescence emission upon 980 nm near infrared excitation.

The morphology of the particles was resolved *via* TEM. The images revealed that the particles are square-like in shape with an average lateral length of 17 ± 3 nm (Fig. 1C). The nanoparticles emit in the violet (400 nm), green (520 to 550 nm), red (650 to 660 nm) and near-infrared (800 to 850 nm) wave-

lengths (Fig. 1D) upon excitation at 980 nm. All the emissions were assigned to the Er^{3+} ion.[41] The particles displayed dominant red emission (Fig. 1D). This was assigned to the exchange energy transfer (ET) processes among Er^{3+} and Mn^{2+} ions,[41] including the nonradiative ET from the $^2H_{9/2}$ and $^4S_{3/2}$ levels of Er^{3+} to the $^4T_1$ level of Mn^{2+}, followed by back-energy transfer (BET) to the $^4F_{9/2}$ level of Er^{3+} (Fig. S2 in the ESI†).

We assessed the response of the fluorescence emission to the water content in the vicinity of the particles. The photoluminescence of the upconverting particles was measured in different mixtures of ethanol and water (Fig. 2A). The intensity of the red band strongly decreased with the concentration of water (Fig. 2A and B), up to 66-fold. The green bands remained almost unchanged (Fig. 2A and B). These results indicate that the excitation source (980 nm) was attenuated by water (Fig. S3 in the ESI†), and in addition, there was a direct ET process among the nanoparticles and water. On typical Er^{3+}-doped upconverting particles (without Mn^{2+} as mediators), a linear quench of the luminescence of the Er^{3+} ion is expected due to a direct multi-phonon relaxation process from the electronic transitions involved in the generation of the green emissions.[44] In our design of nanoparticles, the red emission was expected to be affected more by the changes in the humidity because its heavy doping enables additional quenching mechanisms such as energy migration and cross-relaxations.[45] Excitation paths and quenching mechanisms for the highly doped cubic phase are not entirely understood yet. The optical properties of transition metals are strongly affected by the crystal field of the ligands surrounding them.[46]

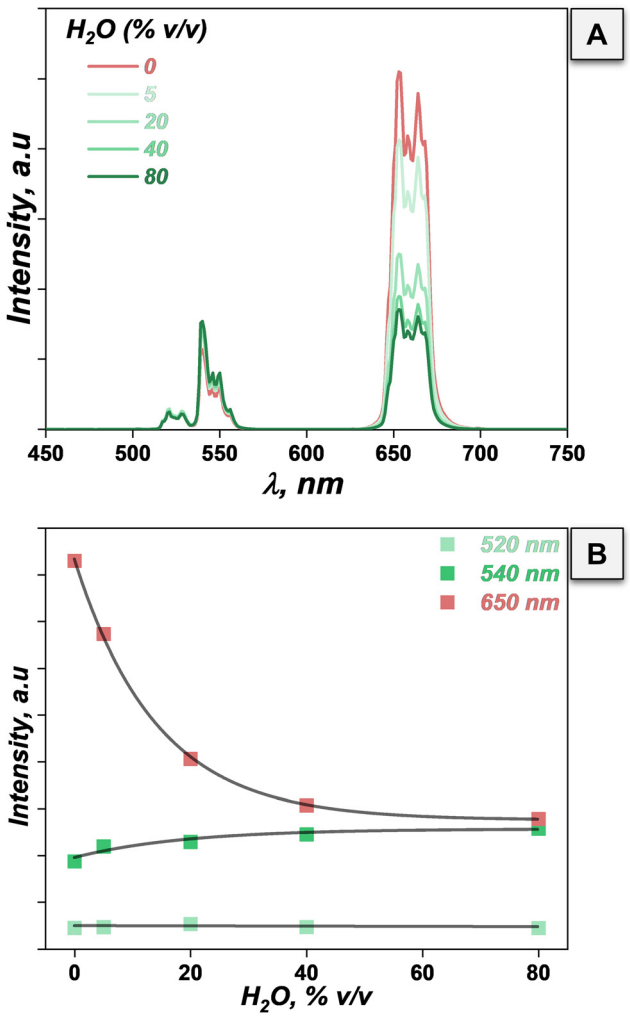

Fig. 2 Humidity-dependent photoluminescence of Mn^{2+}-doped Er^{3+}, Yb^{3+}:$NaYF_4$ nanoparticles in water–ethanol mixtures. (A) Photoluminescence and (B) integrated areas of the upconverting nanoparticles as a function of water content within an organic solvent.

The next step involves the preparation of fluorescent composites within a matrix, *i.e.*, cellulose acetate. This matrix is biodegradable,[34] and commonly applied in 3D printing technologies.[33] Cellulose acetate is transparent within the visible and infrared range of wavelengths,[47] which implies a minimal effect on the photoluminescence of the upconverting particles. In addition, the matrix has the ability to absorb water,[48] which can quench the photoluminescence.

The fluorescent composites were prepared using a solvent evaporation method.[12] Different concentrations of the upconverting nanoparticles (1–20 wt%) were added to cellulose acetate in acetone. The goal was to produce a stable composite and maximize the signal-to-noise ratio (SNR) of the fluorescent nanoparticles. The dispersions were dropped on a Teflon substrate and dried at room temperature to prepare a white film (Movie S1 in the ESI†). Circular samples of 8.0 ± 0.7 mm in diameter and 200 ± 25 μm in thickness with a mass of 3.3 ± 1.0 mg were punched for testing. A filling ratio of 15 wt% led to composites with a high SNR (Fig. S4 in the ESI†) and with no structural deformation (Fig. 3A). Scanning electron microscopy and EDX confirmed the incorporation of Mn^{2+} ions into the cubic $NaYF_4$ host and a uniform distribution of the nanoparticles within the matrix (Fig. 3B and C). We used EDX spectra to quantify the doping levels and found an atomic ratio of 3 : 5 of Mn^{2+} to Y^{3+} (Table S1 in the ESI†). The photoluminescence of the composite displayed a similar profile as that of the particles (Fig. 3D), implying minimal impact from the matrix (Fig. 3D). Higher concentrations of the nanoparticles, although they increased the intensity of the photoluminescence (Fig. S4 in the ESI†), resulted in increased brittleness, caused agglomeration, and led to fragile films (Fig. S5 in the ESI†).

Production of fluorescent artificial seeds

To properly design the artificial seeds, we collected and resolved the properties of the natural *Ailanthus altissima* seeds. A typical natural *Ailanthus altissima* seed is composed of the capsule (center part) and the main body (Fig. 4 and 5A). The collected seeds were characterized in terms of their morphometric characteristics (summarized in Fig. S6A in the ESI†). The cellular structure of the natural seeds is composed of dead and empty epidermal cells (Fig. 5B). These cells allow the seed to be lightened and descend slowly after abscission from the tree. In terms of their morphometric characteristics, the seeds have longitudinal (L_L) and transversal (L_T) lengths of 51.3 ±

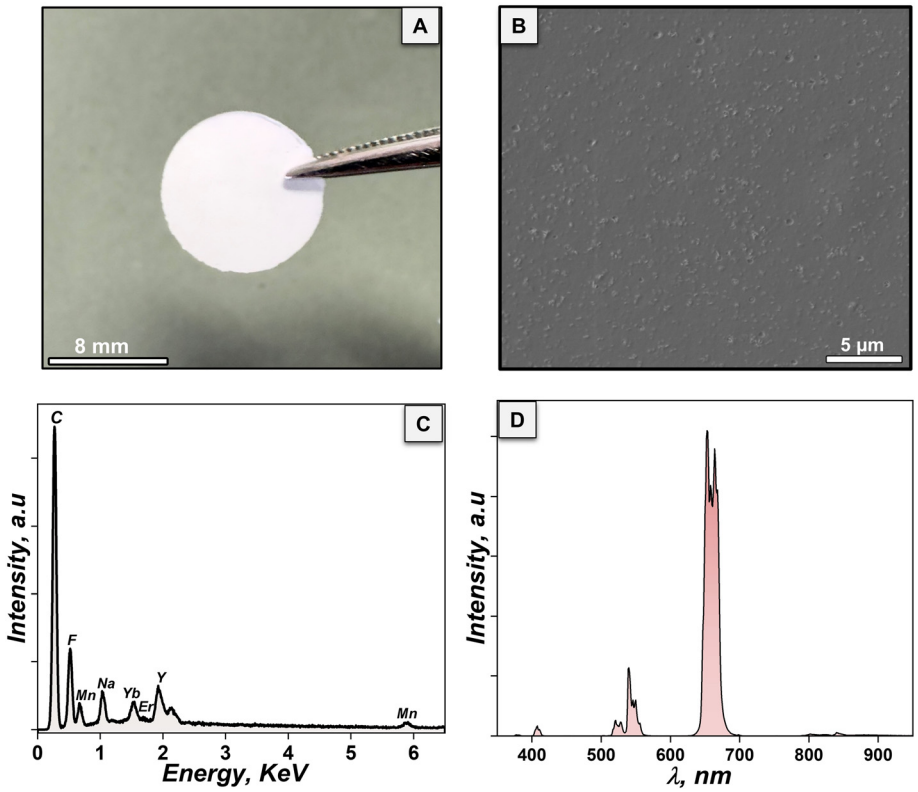

Fig. 3 (A) Digital image, (B) SEM image, (C) EDX spectrum, and (D) photoluminescence under 980 nm irradiation of the fluorescent composite produced *via* the solvent evaporation method.

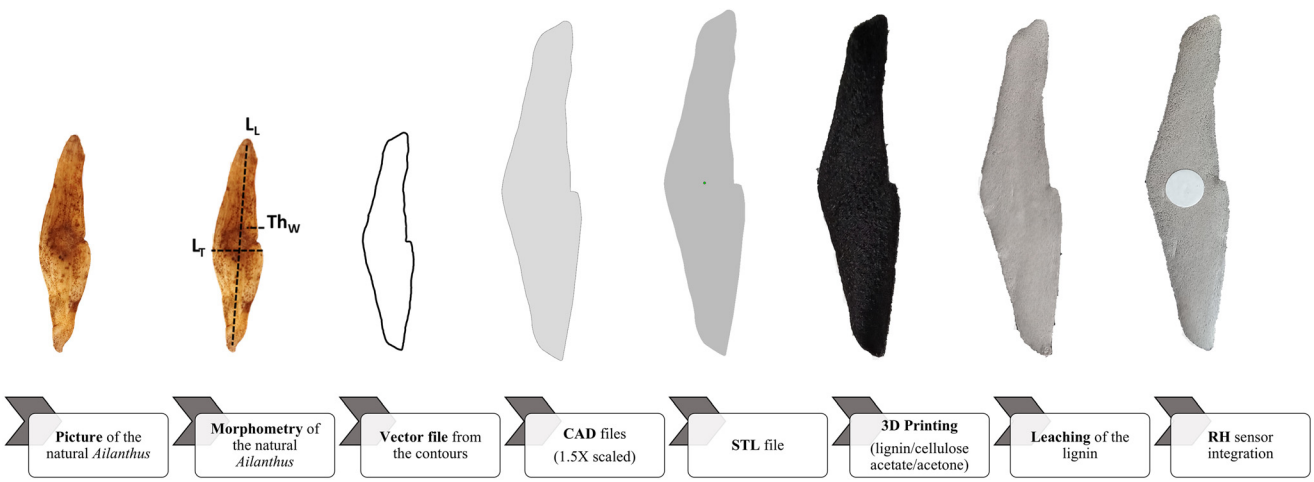

Fig. 4 Development of the artificial seed starting from the natural *Ailanthus altissima* species. The flowchart consists of (i) the picture of natural *Ailanthus altissima*, (ii) morphometric analysis of natural *Ailanthus altissima*, (iii) vector file extract from the contours, (iv) creation of 1.5× scaled CAD files, (v) creation of 1.5× scaled STL files, (vi) 3D printing of 1.5× scaled artificial *Ailanthus altissima* using the lignin/cellulose acetate/acetone suspension, (vii) leaching of the lignin, and (viii) integration of the RH sensor using ethyl cyanoacrylate as glue.

2.6 mm and 9.8 ± 0.6 mm, respectively (Fig. S6A in the ESI†). The thickness of the wing (T_W) was 0.18 ± 0.01 mm. The mean mass (M) of the seed was 25.9 ± 2.6 mg and the mean surface area (S) was around 777 ± 19 mm^2. The computed wing loading (W/S), extracted as the ratio between the weight and the surface, was 0.70 ± 0.11 N m^{-2}. In addition, we determined the descent speed under laboratory conditions (Movie S2 in the ESI†), which was found to be around 0.79 ± 0.10 m s^{-1} in the configuration of the spirally twisted flight (Fig. 5C).

All these characteristics serve as a guideline to produce the artificial seeds. Based on these characteristics, we drew a vectorized contour from a picture of these natural seeds (Fig. 4).

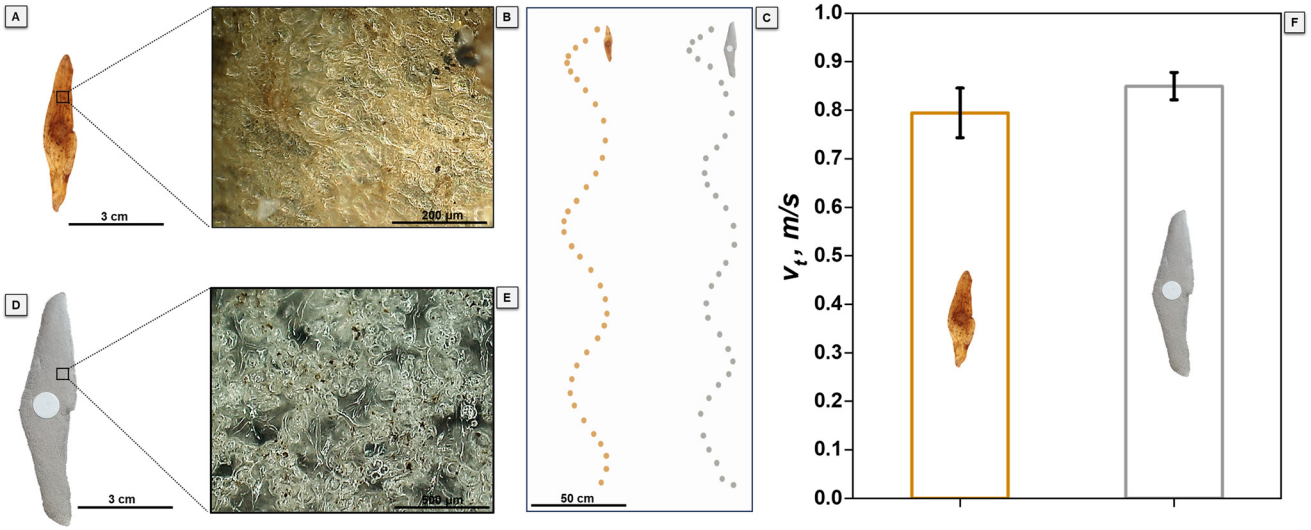

Fig. 5 (A) Picture of a natural *Ailanthus altissima* seed. (B) Optical microscopy image of the surface of the natural seed. (C) Tracking of the spirally twisted falling of natural (orange trace) and artificial *Ailanthus altissima* (grey trace) seeds. (D) Picture of the 1.5× scaled *Ailanthus altissima* seed coupled with the RH sensor (white disc in the centre). (E) Optical microscopy image of the surface of the artificial seed. (F) Bar plot of the descent speed of the natural (orange bar) and artificial (grey bar) seeds.

This contour was transferred to the 3D CAD software. Following this, a model was extruded and scaled up to 1.5× the original dimensions of the natural seeds to allow for a larger area for coupling with the fluorescence sensor. This scaled up design was converted to an STL file to be added into the slicing software of the 3D Bioplotter printer for the final production of the flying seeds (Fig. 4). As a printing material, a mixture of cellulose acetate/lignin/acetone (23/23/54 wt%) was applied, as reported previously.[17] After printing, the *Ailanthus altissima* flier (in black in Fig. 4) underwent a leaching process in water, which removed lignin, leaving a porous cellulose acetate network (in grey in Fig. 4).

The fluorescent composite was attached at both sides of the capsule[17] of the printed *Ailanthus altissima* flier using ethyl cyanoacrylate as a glue (Fig. 4 and 5D). With the addition of a fluorescent composite unit and scaling up the dimensions by 1.5×, the morphometric and aerodynamic characteristics of the flier (composite and printed seeds) were analysed. The artificial seeds (Fig. 4 and 5D) had longitudinal (L_L) and transversal (L_T) lengths of 71.3 ± 1.5 mm and 16.1 ± 0.7 mm, respectively (Fig. S6C and D in the ESI†). The thickness of the wing (T_W) was 0.21 ± 0.01 mm. The artificial seeds were composed of a porous structure with an average value of 68.1 ± 1.1% (Fig. 5E). The total mass (W) of the flier, as the artificial seed and the sensing unit, was 60.4 ± 4.0 mg and the mean surface area (S) was 777 ± 19 mm^2 (Fig. S6C and D in the ESI†). The wing loading (W/S) of the printed flier was 0.76 ± 0.07 N m^{-2}, similar to the natural seeds (*i.e.*, 0.70 ± 0.11 N m^{-2}). We also tested the descent speed of the printed fliers in the same configuration as the natural seeds (spirally twisted flight, Fig. 5C and Movie S2 in the ESI†). The descent speed of the artificial fliers was found to be around 0.85 ± 0.06 m s^{-1}, similar to that of the natural seeds (0.79 ± 0.10 m s^{-1}) (Fig. 5F). These results revealed that it is possible to print fluorescent artificial seeds that mimic the properties of the natural seeds by preserving the same design and wing loading, regardless of the weight, dimensions and addition of the sensing unit.

Fluorescent artificial seeds as humidity sensors

After integrating the composite into the flier and confirming their photoluminescence properties, we tested their functionality as humidity sensors. The flier was exposed to different levels of humidity (dry, 30%, 60% and 95%, experiments conducted in triplicate) at constant room temperature (298 K). The time of exposure was 1 hour for each level of humidity. After exposure, the photoluminescence spectra were recorded (Fig. 6A). We monitored the evolution of the wavelengths with the highest SNR: the green (510 to 560 nm) and red (620 to 700 nm) emissions (Fig. 6A).

With the increase of the levels of the humidity, the upconversion emission within the visible wavelengths was gradually quenched (Fig. 6A). The intensity of the red emission decreased drastically compared to the initial value under dry conditions (Fig. 6B). On the other hand, the intensity of the green emission displayed a steady decrease with the increase of the levels of humidity (Fig. 6B).

We monitored the intensity ratio of these two peaks as a function of the humidity levels, *i.e.*, using ratiometric readouts, to evaluate the performance of these fliers as humidity sensors. This technique is barely affected by the surrounding environment and requires only simple optical setups.[27] Applying the ratio among the intensity of the green and red emissions allows us to extract an empirical equation that describes the conduct of the flier as a function of humidity. It could be deduced that this ratio increases exponentially (with R^2 = 0.998) with the increase of the levels of the humidity

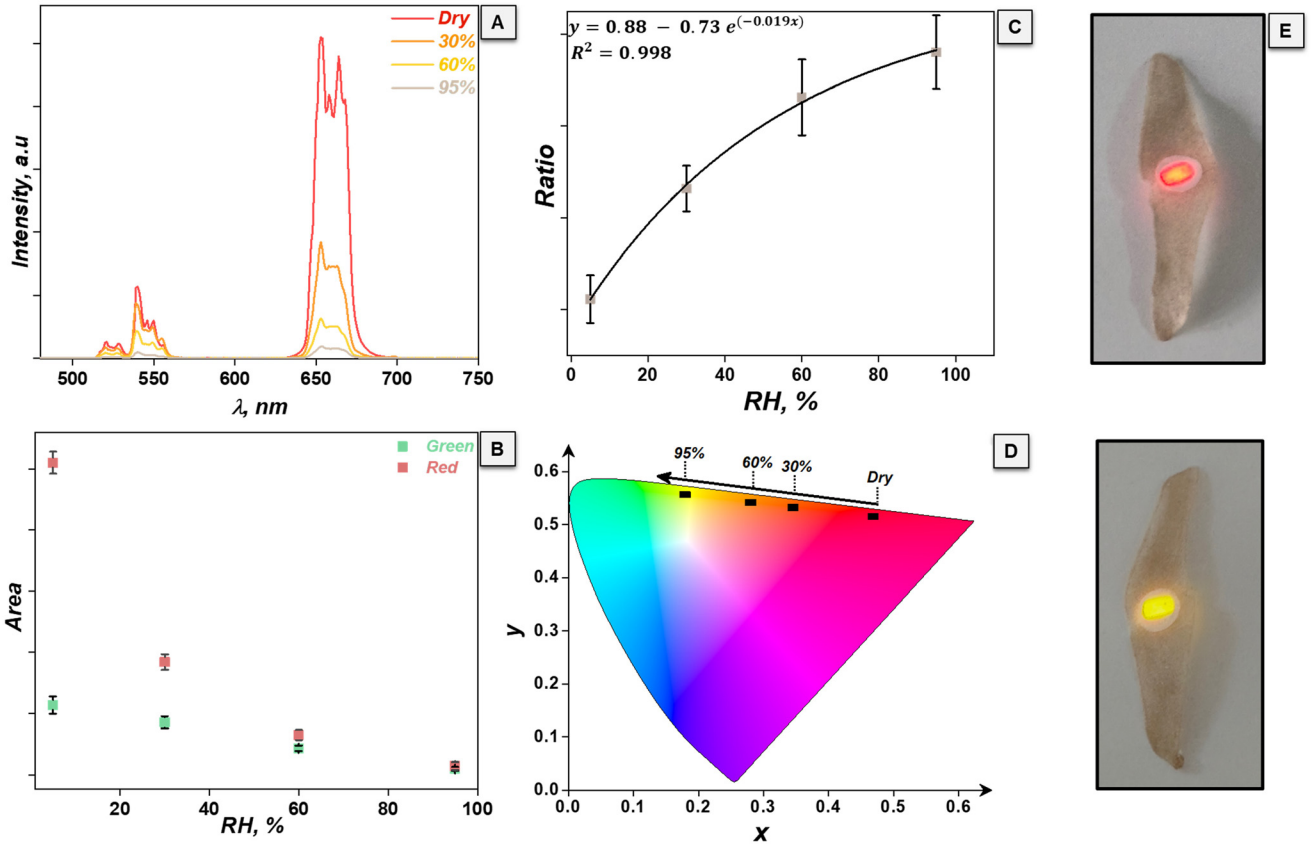

Fig. 6 Fluorescent artificial *Ailanthus altissima* seeds as relative humidity sensors: (A) photoluminescence spectrum, (B) the evolution of the integrated areas of the green and red wavelengths, (C) ratio of the two wavelengths (green/red) as a function of different humidity levels (from dry to 95%) and the fitting equation, (D) CIE coordinates, and (E) digital images of the fluorescent flier before and after being exposed to 95% humidity, irradiated with a 980 nm laser pointer.

(Fig. 6C), displaying a nonlinear quenching effect, as accounted also in the experiments at the nanoparticle's level. Based on the calibration curve, we can calculate the limit of detection (LOD) of our humidity sensors using the following equation reported:[49]

$$\mathrm{LOD} = 10^{\left(\frac{3\sigma}{K}\right)} \quad (1)$$

where σ is the standard deviation of the percentage of change of the intensities of the photoluminescence and K is the slope of the calibration curve. The resulting LOD for our material was at 4.1% RH.

These changes can be expressed as CIE coordinates too (Fig. 6D). A dry flier displays a red color under 980 nm excitation with coordinates x = 0.46 and y = 0.52 (Fig. 6D). With the increase of the humidity levels, the perceived color switches towards the green wavelengths, reaching coordinates of x = 0.16 and y = 0.56 for the maximum humidity of 95% (Fig. 6D). In addition, the change in the color of the photoluminescence could be easily detected by the naked eye. From a clear red emitted color in the dry state (Fig. 6E), after exposure to 95% humidity, the color of the emission gradually changes to yellowish-green (Fig. 6E), in accordance with the spectra and CIE coordinates.

Temperature can quench the intensity of the photoluminescence of lanthanide-doped nanoparticles.[27] When exposed to the range from 273 K to 313 K, the intensities of the 540 nm and 650 nm bands decreased with the increase of the temperature (Fig. S7A and B in the ESI†). The maximum decrease was detected for the red band with a maximum of only 22% (Fig. S7B in the ESI†). The intensity ratio between these two bands displayed a linear increase with temperature (Fig. S7C†), different from the calibration curve under relative humidity (Fig. 6C).

Conclusions

In summary, we were able to 3D print self-deployable and biodegradable fliers inspired by *Ailanthus altissima* seeds. The seeds are composed of an artificial flier and a fluorescent composite attached at the capsule. They emulate the morphometric and aerodynamic characteristics of the natural seeds. The fluorescent composite renders the whole seed as a humidity sensor. The sensing is based on monitoring ratiometrically

the intensity of the photoluminescence in the green and red wavelengths. Further work is required to provide quantitative link between the structural, mechanical and optical properties of the sensing unit as a function of time. In addition, the seeds were built on biodegradable materials, such as cellulose derivatives. In the near future, the developed artificial seeds can be upscaled, designed to sense multiple environmental parameters, and biodegrade faster, inspiring the development of sustainable, porous, and lightweight carriers to be deployed in the environment to be read out with drones equipped with fluorescence light detection and ranging (fLIDAR).

Author contributions

Albenc Nexha and Stefano Mariani wrote the original draft of the manuscript. Albenc Nexha and Thomas Kister performed the experiments on the upconverting nanoparticles, preparation of the composites and humidity sensing. Stefano Mariani and Kliton Cikalleshi worked on the production and characterization of the artificial seeds. All authors took part in the conceptualization, reviewing, and editing of the manuscript. Barbara Mazzolai and Tobias Kraus led the supervision and funding acquisition.

Conflicts of interest

There are no conflicts to declare.

Data availability

The data that support the findings of this study will be made available from the corresponding authors, Barbara Mazzolai and Tobias Kraus, upon request.

Acknowledgements

This project has received funding from the European Union's Horizon 2020 research and innovation program under grant agreement no. 101017940 (I-Seed).

References

1 M. Ikram, S. Ameer, F. Kulsoom, M. Sher, A. Ahmad, A. Zahid and Y. Chang, *Comput. Electron. Agric.*, 2024, **226**, 109449.
2 S. Mariani, L. Cecchini, N. M. Pugno and B. Mazzolai, *Mater. Des.*, 2023, **235**, 112408.
3 V. Montes-García and P. Samorì, *Adv. Mater.*, 2024, **36**, 2208766.
4 P. Wolkoff, *Int. J. Hyg. Environ.*, 2018, **221**, 376–390.
5 N. Goad and D. J. Gawkrodger, *J. Eur. Acad. Dermatol. Venereol.*, 2016, **30**, 1285–1294.
6 A. Kumar and A. K. Attri, *Atmos. Pollut. Res.*, 2016, **7**, 858–864.
7 M. Dokmeci and K. Najafi, *J. Microelectromech. Syst.*, 2001, **10**, 197–204.
8 H. Farahani, R. Wagiran and M. N. Hamidon, *Sensors*, 2014, **14**, 7881–7939.
9 F. Tudorache, I. Petrila, K. Popa and A. M. Catargiu, *Appl. Surf. Sci.*, 2014, **303**, 175–179.
10 W. C. Wang, Y. T. Tian, K. Li, E. Y. Lu, D. S. Gong and X. J. Li, *Appl. Surf. Sci.*, 2013, **273**, 372–376.
11 H. J. Yoon, G. Lee, J. T. Kim, J. Y. Yoo, H. Luan, S. Cheng, S. Kang, H. L. T. Huynh, H. Kim, J. Park, J. Kim, S. S. Kwak, H. Ryu, J. Kim, Y. S. Choi, H. Y. Ahn, J. Choi, S. Oh, Y. H. Jung, M. Park, W. Bai, Y. Huang, L. P. Chamorro, Y. Park and J. A. Rogers, *Sci. Adv.*, 2022, **8**, eade3201.
12 K. Cikalleshi, A. Nexha, T. Kister, M. Ronzan, A. Mondini, S. Mariani, T. Kraus and B. Mazzolai, *Sci. Adv.*, 2023, **9**, eadi8492.
13 M. Seale and N. Nakayama, *New Phytol.*, 2020, **225**, 653–658.
14 V. Iyer, A. Najafi, J. James, S. Fuller and S. Gollakota, *Sci. Rob.*, 2020, **5**, eabb0839.
15 K. Johnson, V. Arroyos, A. Ferran, R. Villanueva, D. Yin, T. Elberier, A. Aliseda, S. Fuller, V. Iyer and S. Gollakota, *Sci. Rob.*, 2023, **8**, eadg4276.
16 V. Iyer, H. Gaensbauer, T. L. Daniel and S. Gollakota, *Nature*, 2022, **603**, 427–433.
17 K. Cikalleshi, S. Mariani and B. Mazzolai, *Biomimetic and Biohybrid Systems*, Cham, 2023, pp. 117–129.
18 B. H. Kim, K. Li, J. T. Kim, Y. Park, H. Jang, X. Wang, Z. Xie, S. M. Won, H. J. Yoon, G. Lee, W. J. Jang, K. H. Lee, T. S. Chung, Y. H. Jung, S. Y. Heo, Y. Lee, J. Kim, T. Cai, Y. Kim, P. Prasopsukh, Y. Yu, X. Yu, R. Avila, H. Luan, H. Song, F. Zhu, Y. Zhao, L. Chen, S. H. Han, J. Kim, S. J. Oh, H. Lee, C. H. Lee, Y. Huang, L. P. Chamorro, Y. Zhang and J. A. Rogers, *Nature*, 2021, **597**, 503–510.
19 J. T. Kim, H. J. Yoon, S. Cheng, F. Liu, S. Kang, S. Paudel, D. Cho, H. Luan, M. Lee, G. Jeong, J. Park, Y. T. Huang, S. E. Lee, M. Cho, G. Lee, M. Han, B. H. Kim, J. Yan, Y. Park, S. Jung, L. P. Chamorro and J. A. Rogers, *PNAS Nexus*, 2024, **3**, 110.
20 S. Mariani, K. Cikalleshi, M. Ronzan, C. Filippeschi, G. A. Naselli and B. Mazzolai, *Small*, 2025, **21**, 2403582.
21 F. Wiesemüller, Z. Meng, Y. Hu, A. Farinha, Y. Govdeli, P. H. Nguyen, G. Nyström and M. Kovač, *Front. Rob. AI*, 2022, **9**, 1011793–1011808.
22 B. Mazzolai, S. Mariani, M. Ronzan, L. Cecchini, I. Fiorello, K. Cikalleshi and L. Margheri, *Front. Rob. AI*, 2021, **8**, 797556–797563.
23 L. Cecchini, S. Mariani, M. Ronzan, A. Mondini, N. M. Pugno and B. Mazzolai, *Adv. Sci.*, 2023, **10**, 2205146.
24 B. J. Johnson, A. P. Malanoski and J. S. Erickson, *Sensors*, 2020, **20**, 5857.
25 S. Wu, T. Liu, B. Tang, L. Li and S. Zhang, *ACS Appl. Mater. Interfaces*, 2019, **11**, 10171–10177.

26 B. A. Kuzubasoglu, *ACS Appl. Electron. Mater.*, 2022, **4**, 4797–4807.
27 A. Nexha, J. J. Carvajal, M. C. Pujol, F. Díaz and M. Aguiló, *Nanoscale*, 2021, **13**, 7913–7987.
28 C. D. S. Brites, P. P. Lima, N. J. O. Silva, A. Millán, V. S. Amaral, F. Palacio and L. D. Carlos, *Nanoscale*, 2012, **4**, 4799–4829.
29 A. Nexha, M. C. Pujol Baiges and J. J. Carvajal Martí, in *Luminescent Thermometry: Applications and Uses*, ed. J. J. Carvajal Martí and M. C. Pujol Baiges, Springer International Publishing, Cham, 2023, pp. 221–268. DOI: 10.1007/978-3-031-28516-5_6.
30 A. Gnach, T. Lipinski, A. Bednarkiewicz, J. Rybka and J. A. Capobianco, *Chem. Soc. Rev.*, 2015, **44**, 1561–1584.
31 P. Peng, N. Wu, L. Ye, F. Jiang, W. Feng, F. Li, Y. Liu and M. Hong, *ACS Nano*, 2020, **14**, 16672–16680.
32 A. Nexha, J. J. Carvajal, M. C. Pujol, F. Díaz and M. Aguiló, *J. Mater. Chem. C*, 2021, **9**, 2024–2036.
33 S. W. Pattinson and A. J. Hart, *Adv. Mater. Technol.*, 2017, **2**, 1600084.
34 J. Puls, S. A. Wilson and D. Hölter, *J. Environ. Polym. Degrad.*, 2011, **19**, 152–165.
35 N. Yadav and M. Hakkarainen, *Macromol. Mater. Eng.*, 2022, **307**, 2100951.
36 E. Rudnik, in *Compostable Polymer Materials (Second Edition)*, ed. E. Rudnik, Elsevier, Boston, 2019, pp. 255–292. DOI: 10.1016/B978-0-08-099438-3.00008-2.
37 W. C. Thomas, L. F. McGrath, K. A. Baarson, C. S. Auletta, I. W. Daly and R. F. McConnell, *Food Chem. Toxicol.*, 1991, **29**, 453–458.
38 I. Kowarik and I. Säumel, *Perspect. Plant Ecol. Evol. Syst.*, 2007, **8**, 207–237.
39 G. R. Matlack, *Am. J. Bot.*, 1987, **74**, 1150–1160.
40 L. Vincent, Y. Liu and E. Kanso, *J. Fluid Mech.*, 2020, **889**, A9.
41 G. Tian, Z. Gu, L. Zhou, W. Yin, X. Liu, L. Yan, S. Jin, W. Ren, G. Xing, S. Li and Y. Zhao, *Adv. Mater.*, 2012, **24**, 1226–1231.
42 W. Kong, T. Sun, B. Chen, X. Chen, F. Ai, X. Zhu, M. Li, W. Zhang, G. Zhu and F. Wang, *Inorg. Chem.*, 2017, **56**, 872–877.
43 C. A. Schneider, W. S. Rasband and K. W. Eliceiri, *Nat. Methods*, 2012, **9**, 671–675.
44 F. T. Rabouw, P. T. Prins, P. Villanueva-Delgado, M. Castelijns, R. G. Geitenbeek and A. Meijerink, *ACS Nano*, 2018, **12**, 4812–4823.
45 J. Zuo, W. Wang, D. Zhang, X. Wang, Y. Ma, P. Li, Y. Li, W. Sun, Y. Zhang, L. Tu, Y. Chang, Q. Li and H. Zhang, *Appl. Surf. Sci.*, 2022, **575**, 151701.
46 M. Dramićanin, in *Luminescence Thermometry*, ed. M. Dramićanin, Woodhead Publishing, 2018, pp. 113–157. DOI: 10.1016/B978-0-08-102029-6.00006-3.
47 M. E. Culica, A. L. Chibac-Scutaru, V. Melinte and S. Coseri, *Materials*, 2020, **13**, 2955.
48 G. Mensitieri and G. Scherillo, in *Wiley Encyclopedia of Composites*, 2012, pp. 1–25. DOI: 10.1002/9781118097298.weoc074.
49 J. Zuo, W. Wang, D. Zhang, X. Wang, Y. Ma, P. Li, Y. Li, W. Sun, Y. Zhang, L. Tu, Y. Chang, Q. Li and H. Zhang, *Appl. Surf. Sci.*, 2022, **575**, 151701.